NASA Contractor Report 187071

Calculations of Steady and Transient Channel Flows With a Time-Accurate L-U Factorization Scheme

S.-W. Kim
University of Texas at Arlington
Arlington, Texas

August 1991

Prepared for
Lewis Research Center
Under Cooperative Agreement NCC3 - 180

National Aeronautics and
Space Administration

CALCULATIONS OF STEADY AND TRANSIENT CHANNEL FLOWS WITH A TIME-ACCURATE L-U FACTORIZATION SCHEME

S.-W. Kim*
University of Texas at Arlington
Department of Aerospace Engineering
Arlington, Texas 76010

SUMMARY

Calculations of steady and unsteady, transonic, turbulent channel flows with a time-accurate, lower-upper (L-U) factorization scheme are presented. The L-U factorization scheme is formally second-order accurate in time and space, and it is an extension of the steady state-flow solver (RPLUS) used extensively to solve compressible flows. A time-discretization method and the implementation of a consistent boundary condition specific to the L-U factorization scheme are also presented. The turbulence is described by the Baldwin-Lomax algebraic turbulence model. The present L-U scheme yields stable numerical results with the use of much smaller artificial dissipations than those used in the previous steady-flow solver for steady and unsteady channel flows. The capability to solve time-dependent flows is shown by solving very weakly excited and strongly excited, forced oscillatory, channel flows.

INTRODUCTION

In the lower-upper (L-U) factorization scheme (ref. 1), the governing flow equations are factored into forward (lower) and backward (upper) difference operators, and the factored flow equations are solved by an implicit finite volume method. The L-U scheme has a few advantages over other numerical methods for solving compressible flows. In the L-U scheme, only two factored equations need to be solved for any number of physical dimensions, whereas in the Alternating-Direction-Implicit (ADI) schemes, three factored equations need to be solved for three-dimensional flows. Thus, the number of numerical operations and the required memory size are smaller in the L-U schemes. Due to the use of an implicit time-stepping, which is usually free of the Courant-Friedrichs-Lewy (CFL) stability constraint condition, a relatively large time-step can be used in the L-U schemes. Even though the method is implicit, the costly matrix inversion of a large discrete system of equations is minimized, as shown in the following section. Due to the efficiency of the L-U scheme to solve large problems, the method has been rapidly extended to solve chemically reacting flows (ref. 2) and hypersonic flows (ref. 3). The method has also been extended to solve incompressible flows (ref. 4).

Many fluid flows exhibit natural oscillations which may or may not be desirable from the design point of view. In certain cases, fluid flows may go through forced oscillations to achieve certain objectives. The start-up and shut-down of a fluid machinery also impart unsteadiness to the fluid flow, and critical fluid loading may occur during such processes. Therefore, unsteady-flow solvers are more desirable than steady-flow solvers. Furthermore, steady

---

*NASA Resident Research Associate at Lewis Research Center.

flows can also be solved by using unsteady-flow solvers. In this report, the L-U scheme is extended to solve transient flows by incorporating the generalized time-differencing scheme of Beam and Warming (refs. 5 and 6). To correctly resolve the transient flow phenomenon at and near the boundary, the boundary conditions are implemented in predictor and corrector steps in a mathematically consistent form with the time-accurate L-U factorization scheme.

SYMBOLS

$\hat{A}$	Jacobian matrix for $\hat{E}$, $\hat{A} = \{\partial\hat{E}/\partial\hat{Q}\}$
$\hat{B}$	Jacobian matrix for $\hat{F}$, $\hat{B} = \{\partial\hat{F}/\partial\hat{Q}\}$
E,F	convective transport vector
E_v,F_v	diffusive transport vector
H	height of channel throat, (H = 0.044 m)
I	identity matrix
k	effective thermal conductivity
(ℓ,m)	index for mesh
p	pressure
p_e	pressure at the exit boundary
p_t	total pressure
Q	vector of flow variables, $Q = \{\rho,\rho u,\rho v,\rho e\}^T$
R_p	pressure ratio, $R_p = p_e/p_t$
u_j	velocity component, $u_j = \{u,v\}$
x_j	Cartesian coordinates, $x_j = \{x,y\}$
$\Delta\hat{S}$	intermediate solution
θ	phase angle
μ	molecular viscosity
μ_e	effective viscosity
μ_t	turbulent viscosity
ξ_j	curvilinear coordinates, $\xi_j = \{\xi,\eta,\zeta\}$
$\mathcal{O}$	order of magnitude

Superscripts:

n	iteration count
$\hat{}$	vector or matrix defined on curvilinear coordinates

Subscripts:

i,j	index for spatial coordinates, $i = \{1,2,3\}$ and $j = \{1,2,3\}$

L-U FACTORIZATION SCHEME

The time-dependent, compressible, turbulent flow equation is given as

$$\frac{\partial Q}{\partial t} = -\frac{\partial E}{\partial x} - \frac{\partial F}{\partial y} + \frac{\partial E_v}{\partial x} + \frac{\partial F_v}{\partial y} \tag{1}$$

where

$$Q = \{\rho,\ \rho u,\ \rho v,\ \rho e\}^T$$

$$E = \{\rho u,\ \rho u^2 + p,\ \rho uv,\ u(\rho e + p)\}^T$$

$$F = \{\rho v,\ \rho uv,\ \rho v^2 + p,\ v(\rho e + p)\}^T$$

$$E_v = \{0,\ \tau_{xx},\ \tau_{xy},\ u\tau_{xx} + v\tau_{xy} - q_x\}^T$$

$$F_v = \{0,\ \tau_{yx},\ \tau_{yy},\ u\tau_{yx} + v\tau_{yy} - q_y\}^T$$

In the above equations, $\tau_{ij} = 2\mu_e \varepsilon_{ij} + \lambda \varepsilon_{kk} \delta_{ij}$ is the stress tensor, $\varepsilon_{ij} = (\partial u_i/\partial x_j + \partial u_j/\partial x_i)$ is the strain rate tensor, $\mu_e = \mu + \mu_t$ is the effective viscosity, $\lambda = -2/3\mu_e$ is the second viscosity for compressibility, $q_i = -k\partial T/\partial x_i$ is the heat flux due to temperature gradient, and the subscripts i and j denote each coordinate direction. For flows with arbitrary geometries, it is more convenient to solve the flow equation defined on curvilinear coordinates with the use of body-fitted grids than to solve the flow equation defined on cartesian coordinates. The coordinate transformed flow equation can be written as

$$\frac{\partial \hat{Q}}{\partial \tau} = -\frac{\partial \hat{E}}{\partial \xi} - \frac{\partial \hat{F}}{\partial \eta} + \frac{\partial \hat{E}_v}{\partial \xi} + \frac{\partial \hat{F}_v}{\partial \eta} \tag{2}$$

where $\hat{Q} = Q/J$, $\hat{E} = (\xi_x E + \xi_y F + \xi_t Q)/J$, $\hat{F} = (\eta_x E + \eta_y F + \eta_t Q)/J$, $\hat{E}_v = (\xi_x E_v + \xi_y F_v)/J$, $\hat{F}_v = (\eta_x E_v + \eta_y F_v)/J$, J is the grid transformation Jacobian, and ξ_x, ξ_y, η_x, and η_y are grid transformation metrics. A general form time-discretization for $\partial \hat{Q}/\partial \tau$ is given (ref. 5) as

$$\frac{\Delta \hat{Q}^n}{\Delta \tau} = \frac{\theta_1}{1+\theta_2}\frac{\partial \Delta \hat{Q}^n}{\partial \tau} + \frac{1}{1+\theta_2}\frac{\partial \hat{Q}^n}{\partial \tau} + \frac{\theta_2}{1+\theta_2}\frac{\Delta \hat{Q}^{n-1}}{\Delta \tau} + \mathcal{O}\left[\left(\theta_1 - \frac{1}{2} - \theta_2\right)\Delta\tau + (\Delta\tau)^2\right] \tag{3}$$

where the last term represents the truncation error. For the implicit, three-point, backward differencing case used in the present study, $\theta_1 = 1$, $\theta_2 = 1/2$, the temporal truncation error is $\mathcal{O}(\Delta\tau)^3$, $\Delta \hat{Q}^n = \hat{Q}^{n+1} - \hat{Q}^n$, and equation (3) is an alternative form of

$$\frac{\partial \hat{Q}}{\partial \tau} = \frac{3\hat{Q}^{n+1} - 4\hat{Q}^{n} + \hat{Q}^{n-1}}{2\Delta\tau} = \frac{3(\Delta\hat{Q})^{n} - (\Delta\hat{Q})^{n-1}}{2\Delta\tau}$$

Solving equation (2) for $\partial\hat{Q}^n/\partial\tau$ and $\partial\Delta\hat{Q}^n/\partial\tau$ and substituting the results into equation (3) yields

$$\Delta\hat{Q}^{n} + \frac{\theta_1\Delta\tau}{1+\theta_2}\left(\frac{\partial\Delta\hat{E}^{n}}{\partial\xi} + \frac{\partial\Delta\hat{F}^{n}}{\partial\eta}\right) = \hat{R} \tag{4}$$

where

$$\hat{R} = \frac{\Delta\tau}{1+\theta_2}\left(-\frac{\partial\hat{E}^{n}}{\partial\xi} - \frac{\partial\hat{F}^{n}}{\partial\eta}\right) + \frac{(1+\theta_1)\Delta\tau}{1+\theta_2}\left(\frac{\partial\hat{E}_v^{n}}{\partial\xi} + \frac{\partial\hat{F}_v^{n}}{\partial\eta}\right)$$

$$- \frac{\theta_1\Delta\tau}{1+\theta_2}\left(\frac{\partial\hat{E}_v^{n-1}}{\partial\xi} + \frac{\partial\hat{F}_v^{n-1}}{\partial\eta}\right) + \frac{\theta_2}{1+\theta_2}\Delta\hat{Q}^{n-1}$$

In deriving the residual function ($\hat{R}$), $\Delta\hat{E}_v^n$ and $\Delta\hat{F}_v^n$ are approximated as $\Delta\hat{E}_v^{n-1}\left(=\hat{E}_v^{n} - \hat{E}_v^{n-1}\right)$ and $\Delta\hat{F}_v^{n-1}\left(=\hat{F}_v^{n} - \hat{F}_v^{n-1}\right)$. In the ADI schemes (refs. 5 and 6) using the same time-discretization method (ref. 5), the time-lag approximation is used only for the cross-derivatives of the viscous transport terms. In the present case, all the viscous transport terms are lagged by one time step to facilitate the L-U factorization. The errors involved in these approximations are $\mathcal{O}(\Delta\tau)^2$, and hence the formal accuracy of the scheme remains intact (ref. 5). The convective transport terms in equation (4) are nonlinear functions of the flow variables. To solve equation (4) by a numerical method, the nonlinear terms are linearized as

$$\left.\begin{aligned}\Delta\hat{E}^{n} &= \hat{A}\Delta\hat{Q}^{n} + \mathcal{O}(\Delta\tau)^2\\ \Delta\hat{F}^{n} &= \hat{B}\Delta\hat{Q}^{n} + \mathcal{O}(\Delta\tau)^2\end{aligned}\right\} \tag{5}$$

where $\hat{A} = \partial\hat{E}^n/\partial\hat{Q}$ and $\hat{B} = \partial\hat{F}^n/\partial\hat{Q}$ are the Jacobian matrices. Substituting equation (5) into equation (4) yields

$$\Delta\hat{Q} + \frac{\theta_1\Delta\tau}{1+\theta_2}\left(\frac{\partial\hat{A}}{\partial\xi} + \frac{\partial\hat{B}}{\partial\eta}\right)\Delta\hat{Q} = \hat{R} \tag{6}$$

where the superscript n has been deleted for notational convenience. For the L-U factorization of equation (6), the Jacobian matrices are decomposed as

$$\left.\begin{aligned}\hat{A} &= \hat{A}^{+} + \hat{A}^{-} \\ \hat{A} &= \hat{A}^{+} + \hat{A}^{-}\end{aligned}\right\} \tag{7}$$

where $\hat{A}^{+} = 1/2(\hat{A} + r_A I)$, $\hat{A}^{-} = 1/2(\hat{A} - r_A I)$, $\hat{B}^{+} = 1/2(\hat{B} + r_B I)$, $\hat{B}^{-} = 1/2(\hat{B} - r_B I)$, $r_A > \max(|\nu_B|)$ and $r_B > \max(|\nu_B|)$, and ν_A and ν_B are the eigen values of the Jacobian matrices $\hat{A}$ and $\hat{B}$, respectively. The eigen values of $\hat{A}^{+}$ and $\hat{B}^{+}$ matrices are positive values, and the eigen values of $\hat{A}^{-}$ and $\hat{B}^{-}$ matrices are negative values. Inserting equation (7) into equation (6) yields

$$\left[I + \frac{\theta_1 \Delta\tau}{+\theta_2}\left(\frac{\partial^{-}}{\partial\xi}\hat{A}^{+} + \frac{\partial^{-}}{\partial\eta}\hat{B}^{+} + \frac{\partial^{+}}{\partial\xi}\hat{A}^{-} + \frac{\partial^{+}}{\partial\eta}\hat{B}^{-}\right)\right]\Delta\hat{Q} = \hat{R} \tag{8}$$

where $\partial(\hat{A}^{+} + \hat{A}^{-})/\partial\xi$ has been approximated as $\partial^{-}\hat{A}^{+}/\partial\xi + \partial^{+}\hat{A}^{-}/\partial\xi$, $\partial^{-}\hat{A}^{+}/\partial\xi = \hat{A}^{+}(\ell,m) - \hat{A}^{+}(\ell - 1,m)$ is the backward difference operator and $\partial^{+}\hat{A}^{-}/\partial\xi = \hat{A}^{-}(\ell + 1,m) - \hat{A}^{-}(\ell,m)$ is the forward difference operator. The same approximation is also applied to $\partial(\hat{B}^{+} + \hat{B}^{-})/\partial\eta$. After some rearrangement, equation (8) becomes

$$\left[I + \frac{\theta_1 \Delta\tau}{1 + \theta_2}\left(\hat{A}^{+}(\ell,m) - \hat{A}^{-}(\ell,m) - \hat{A}^{+}(\ell,m) + \hat{A}^{-}(\ell + 1,m) + \hat{B}^{+}(\ell,m) - \hat{B}^{-}(\ell,m) - \hat{B}^{+}(\ell,m - 1) + \hat{B}^{-}(\ell,m + 1)\right)\right]\Delta\hat{Q} = \hat{R}$$

or

$$\begin{aligned}&\left\{\left[I + \frac{\theta_1 \Delta\tau}{1 + \theta_2}(r_A + r_B)\right]I - \frac{\theta_1 \Delta\tau}{1 + \theta_2}\left[\hat{A}^{+}(\ell - 1,m) + \hat{B}^{+}(\ell,m - 1)\right]\right\} \\ &\qquad\left\{\left[1 + \frac{\theta_1 \Delta\tau}{1 + \theta_2}(r_A + r_B)\right]I + \frac{\theta_1 \Delta\tau}{1 + \theta_2}\left[\hat{A}^{-}(\ell + 1,m) + \hat{B}^{-}(\ell,m + 1)\right]\right\}\Delta\hat{Q} \\ &\qquad = \left[1 + \frac{\theta_1 \Delta\tau}{1 + \theta_2}(r_A + r_B)\right]\hat{R} + \left(\frac{\theta_1 \Delta\tau}{1 + \theta_2}\right)^2\left[\hat{A}^{+}(\ell - 1,m) + \hat{B}^{+}(\ell,m - 1)\right] \\ &\qquad\quad \times \left[\hat{A}^{-}(\ell + 1,m) + \hat{B}^{-}(\ell,m + 1)\right]\Delta\hat{Q}\end{aligned} \tag{9}$$

where $\hat{A}^+ - \hat{A}^- = r_A I$ and $\hat{B}^+ - \hat{B}^- = r_B I$ have been made use of in deriving equation (9). The last term in equation (9) represents the factorization error. The factorization error shares the same order of accuracy as those of various ADI factorization schemes (refs. 5 and 6). The L-U factored flow equation (eq. (9)) is solved in two steps:

$$\left\{\left[1 + \frac{\theta_1 \Delta\tau}{1 + \theta_2}(r_A + r_B)\right] I - \frac{\theta_1 \Delta\tau}{1 + \theta_2}\left[\hat{A}^+(\ell - 1,m) + \hat{B}^+(\ell,m - 1)\right]\right\}\Delta\hat{S} = \left[1 + \frac{\theta_1 \Delta\tau}{1 + \theta_2}(r_A + r_B)\right]\hat{R} \tag{10}$$

and

$$\left\{\left[1 + \frac{\theta_1 \Delta\tau}{1 + \theta_2}(r_A + r_B)\right] I + \frac{\theta_1 \Delta\tau}{1 + \theta_2}\left[\hat{A}^-(\ell + 1,m) + \hat{B}^-(\ell,m + 1)\right]\right\}\Delta\hat{Q} = \Delta\hat{S} \tag{11}$$

where ΔS is the vector of intermediate solution. In the L-U factorization scheme, only two factored operators need to be solved for any number of physical dimensions; whereas in ADI schemes, three factored operators need to be solved for three-dimensional flows. Thus, less memory and computer time are required in the L-U schemes than in the ADI schemes. For flow equations without source terms (e.g., without chemical reactions), equations (10) and (11) are solved by forward and backward sweeps only; and the costly matrix inversion of a large discrete system of equations is unnecessary.

CONSISTENT BOUNDARY CONDITION

Usually, the boundary conditions in flow problems are given in terms of velocity, pressure and temperature; whereas the flow variables solved for in the present L-U scheme are the density, velocity, and internal energy. Thus, the boundary conditions given in terms of velocity, pressure, and temperature need to be recast in terms of density, velocity, and internal energy. Also note that the boundary conditions to be supplied in the lower sweep (see eq. (10)) need to be prescribed in terms of the intermediate solution on the boundary grid points. To correctly resolve time-dependent boundary conditions, the boundary conditions are implemented in predictor and corrector steps in the present L-U scheme.

Predictor Step for Lower-Sweep

The grid layout near the lower-sweep boundary is shown in figure 1. The intermediate solution on the west boundary or on the south boundary is obtained by using equation (11) and the three incremental solutions at the grid points $\Delta\hat{Q}(\ell,m)$, $\Delta\hat{Q}(\ell + 1,m)$, and $\Delta\hat{Q}(\ell,m + 1)$ shown in figure 1(c). The

incremental solutions at the grid points $(\ell + 1,m)$ and $(\ell,m + 1)$ are predicted as

$$\left.\begin{aligned}\Delta\hat{Q}(\ell + 1,m) &= \hat{Q}^{n}(\ell + 1,m) - \hat{Q}^{n-1}(\ell + 1,m)\\ \Delta\hat{Q}(\ell + 1,m) &= \hat{Q}^{n}(\ell + 1,m) - \hat{Q}^{n-1}(\ell + 1,m)\end{aligned}\right\} \tag{12}$$

The incremental solution at the grid point (ℓ,m), or the grid point b in figure 1(d), is obtained from the boundary conditions and the flow variables of the most current time level. For example, by using the dependent variables, the temperature can be expanded as

$$T = T^{\circ} + \frac{\partial T}{\partial \rho}\Delta\rho + \frac{\partial T}{\partial(\rho u)}\Delta(\rho u) + \frac{\partial T}{\partial(\rho v)}\Delta(\rho v) + \frac{\partial T}{\partial(\rho e)}\Delta(\rho e) \tag{13}$$

For fixed temperature on the wall, the above equation can be rewritten as

$$\left[\frac{\partial T}{\partial \rho}, \frac{\partial T}{\partial(\rho u)}, \frac{\partial T}{\partial(\rho v)}, \frac{\partial T}{\partial(\rho e)}\right][\Delta\rho, \Delta(\rho u), \Delta(\rho v), \Delta(\rho e)]^{T} = T^{\circ} - T^{n} \tag{14}$$

where T° is the prescribed temperature which may or may not depend on time. For prescribed temperature gradient on the boundary, for the second-order one-sided difference approximation case, equation (13) can be rewritten as

$$\frac{\partial T}{\partial n} = \frac{1}{2}(3T_b - 4T_c + T_a) = T_{\eta}^{\circ}$$

or

$$\begin{aligned}&\frac{3}{2}\left[\frac{\partial T}{\partial \rho}, \frac{\partial T}{\partial(\rho u)}, \frac{\partial T}{\partial(\rho v)}, \frac{\partial T}{\partial(\rho e)}\right]_b [\Delta\rho, \Delta(\rho u), \Delta(\rho v), \Delta(\rho e)]_b^{T}\\ &- \frac{4}{2}\left[\frac{\partial T}{\partial \rho}, \frac{\partial T}{\partial(\rho u)}, \frac{\partial T}{\partial(\rho v)}, \frac{\partial T}{\partial(\rho e)}\right]_c [\Delta\rho, \Delta(\rho u), \Delta(\rho v), \Delta(\rho e)]_c^{T}\\ &+ \frac{1}{2}\left[\frac{\partial T}{\partial \rho}, \frac{\partial T}{\partial(\rho u)}, \frac{\partial T}{\partial(\rho v)}, \frac{\partial T}{\partial(\rho e)}\right]_a [\Delta\rho, \Delta(\rho u), \Delta(\rho v), \Delta(\rho e)]_a^{T}\\ &\qquad = T_{\eta}^{\circ} - \left(\frac{3}{2}T_b^{n} - \frac{4}{2}T_c^{n} - \frac{1}{2}T_a^{n}\right)\end{aligned} \tag{15}$$

where the first, second, and third terms of equation (15) are evaluated at grid points b, c, and a, respectively (see fig. 1(d)). Derivation of the discrete boundary conditions for velocity and pressure follows the same

procedure as that for temperature. The discrete boundary condition can be written as

$$\hat{e}_a \Delta\hat{Q}_a + \hat{e}_b \Delta\hat{Q}_b + \hat{e}_c \Delta\hat{Q}_c = \hat{f} \tag{16}$$

where $\hat{e} = \partial(T,u,v,p)/\partial(\rho,\rho u,\rho v,\rho e)$ is the Jacobian matrix. The incremental solution at the boundary grid point, ΔQ_b, is obtained as

$$\Delta\hat{Q}_b = \hat{e}_b^{-1}(\hat{f} - \hat{e}_a \Delta\hat{Q}_a + \hat{e}_c \Delta\hat{Q}_c) = \Delta\hat{Q}(\ell,m) \tag{17}$$

Substituting equations (12) and 17) into equation (11) yields the boundary condition to be used in equation (10).

Predictor Step for Upper-Sweep and Corrector Step

For the upper sweep, the boundary condition on the east and north boundaries are obtained by applying equation (17) for each grid point on the boundary. For each time level, after lower and upper sweeps, the flow variables on the boundary are corrected by using equation (17).

NUMERICAL RESULTS AND DISCUSSION

The geometry of the two-dimensional channel flows considered in the present study is shown in figure 2. Measured data for steady flow cases can be found in references 7 to 9. For R_p (= p_e/p_t) = 0.82, a mild normal shock appears in the downstream region of the throat. The flow field remains almost steady, and flow separation is not observed (ref. 7). For R_p = 0.72, a stronger normal shock than that for R_p = 0.82 appears in the farther downstream region of the throat, and shock-induced separation occurs on the bottom and top walls (ref. 7). The flow for R_p = 0.72 exhibits a mild self-excited oscillatory motion. In the forced oscillation case, a triangular rotor, located at x=13H downstream of the throat, is turned at 100 revolutions per second. Thus, the flow is subjected to a variable exit pressure with the frequency of 300 Hz (refs. 7 and 8). The root-mean-square value of the first harmonic oscillatory pressure at x = 8.65H is approximately 0.57 percent of the local static pressure (refs. 7 and 8). However, the exact time-dependent exit pressure is not given in references 7 and 8. Hence, in the present study, the transient flow calculations are made by using harmonically varying exit pressure, as is done in references 9 and 10.

In numerical calculations, for both steady and unsteady flows, the inlet boundary is located at 4H upstream of the nozzle throat, and the exit boundary is located at 12H downstream of the throat. The entire flow domain is discretized by 113x81 grid points with the concentration of grid points in the near-wall and throat regions. The mesh for the contoured nozzle is shown in figure 3. The first grid point from the wall is located at $y^+ \approx 1$ (i.e., $y/H = 0.651\times10^{-3}$ at the throat). The grid size in the transverse direction is increased by a factor of approximately 1.2. The mean velocities, static pressure, and temperature are prescribed at the inlet boundary. The static

pressure (time-dependent static pressure for unsteady flow) is prescribed at the exit boundary, and the velocities and the temperature are obtained by extrapolation. On the solid walls, no slip boundary condition is used for velocities, and vanishing gradient boundary condition is used for the pressure and temperature. The discrete system of equations is obtained by central differencing, and the numerical instability is suppressed by incorporating an artificial dissipation (ref. 11). The second- and fourth-order artificial dissipation coefficients used are 1/16 and 1/1280, respectively. These artificial dissipation coefficients are much smaller than those used in the L-U factorization scheme for steady flows (refs. 2 and 3) and those used in the ADI schemes (refs. 6 and 11). For steady flows, the present method yields stable numerical results for the CFL number up to approximately 2000. The maximum CFL number that can be used to obtain stable numerical results is approximately one order of magnitude greater than those used in other numerical methods (refs. 1 and 6). The unsteady flows are solved using the CFL number of 20. The capability to obtain stable numerical results by using a very small artificial dissipation and a large time-step is attributed to the time-accurate L-U factorization scheme. For steady flows, the converged solutions are obtained in approximately 2000 time steps.

The turbulence is described by the Baldwin-Lomax turbulence model (ref. 12). It is known that the algebraic turbulence model may not yield accurate numerical results for largely separated flows (ref. 13). The present numerical calculations also reproduce the generally known shortcomings of the turbulence model. These shortcomings are discussed in more detail later in this section.

The calculated pressure and Mach number contours for $R_p = 0.82$ are shown in figure 4, where the incremental pressure and the incremental Mach number between the contour lines are constant. In figure 5, the pressure distributions on the bottom and top walls are compared with the measured data of reference 7 and the numerical results of reference 9. The present numerical results are in good agreement with the measured data in most of the flow region except near $x \approx 4.5H$ on the top wall. The lower pressure distribution in this region is caused by a small recirculation bubble located on the top wall at $x \approx 4.5H$. The recirculation bubble was not observed in the experiment (ref. 7). In the numerical calculation, the reversed flow region is caused by the algebraic turbulence model, which cannot accurately predict the rapidly growing turbulence intensity along the curved surface. In reference 9, the turbulence was described by the k-ω turbulence model, which did not show the reversed flow region.

The calculated mean velocity profiles are shown in figure 6. The calculated mean velocity profile at $x = 1.73H$ is in good agreement with the measured data and the other numerical result (ref. 9). Near and in the downstream region of the spurious separation bubble, the present numerical results compare less favorably with the measured data than do the other numerical results.

The calculated pressure and Mach number contours for $R_p = 0.72$ are shown in figure 7. Again, the incremental pressure and the incremental Mach number between the contour lines are constant. It can be seen in the figure that the shock is moved further in the downstream direction and that the Mach number decreases more rapidly across the shock than the previous case ($R_p = 0.82$) due

to the stronger shock. The calculated pressure distributions on the bottom and top walls are shown in figure 8. The calculated flow field contains a large shock-separated recirculation zone on the top wall and a small shock-separated recirculation zone on the bottom wall. The relatively large discrepancy between the calculated and the measured wall pressure distributions is caused by the large internal blockage formed by the recirculation bubbles. In reference 10, the exit boundary was located at 8.64H downstream of the nozzle throat. In their calculation using the original k-ω turbulence model, the reversed flow region extended beyond the exit boundary and converged solution was not obtained. The converged solution was obtained by using a different turbulence model constant in reference 10. The use of a different turbulence model constant effectively reduces the size of the recirculation bubble and yields numerical results which are in good agreement with the measured data (ref. 10). The same turbulence model that was used in reference 10 has also been used in reference 9. In the present calculation using the Baldwin-Lomax turbulence model, a converged solution cannot be obtained if the exit boundary is located at 8.64H downstream of the nozzle, since the reversed flow region extends beyond the exit boundary. The converged solution is obtained by locating the exit boundary at 12H downstream of the nozzle throat instead of optimizing the Baldwin-Lomax turbulence model.

The calculated mean velocity profiles for $R_p = 0.72$ are shown in figure 9. The calculated mean velocity profiles show a large reversed flow region near the top wall boundary. Near and downstream of the separation region, the present numerical results compare less favorably with the measured data than do the numerical results of reference 9. The present numerical results, as well as those of reference 10, strongly demonstrate that an accurate numerical result can hardly be obtained without the use of a good turbulence model. However, the present study is limited to the development and verification of the time-accurate L-U factorization scheme, and optimization of the algebraic turbulence model is not attempted.

The evolution of flow variables in time for mildly and strongly excited unsteady channel flows are shown in figures 10 and 11, respectively. The exit pressure is prescribed as

$$p_e = p_o + p_c \sin(2\pi f t)$$

where t represents time. For the mildly excited case, $P_o = 0.82$, $P_c = 0.0082$, and $f = 300$; and for the strongly excited case, $p_o = 0.77$, $p_c = 0.05$, and $f = 300$. In each case, the numerical results show that the fluid motion consists of the low-frequency natural oscillation (which is inherent to each flow system) and the forced oscillation. The oscillatory motion of the separation bubble for the strongly excited case is shown in figure 12. As the exit pressure is increased, the separation bubble becomes bigger and moves toward the throat; and as the exit pressure is decreased, the bubble becomes smaller and moves toward the exit boundary. Thus, the numerical method reproduces the experimentally observed trend of the fluid motion.

SUMMARY OF RESULTS

Numerical calculations of steady and forced oscillatory transonic turbulent flows in a two-dimensional channel are made by using a time-accurate L-U factorization scheme. The calculated velocity profiles and the pressure distributions on the walls for the steady flows are in good agreement with the measured data, considering the limited predictive capability of the algebraic turbulence model for complex turbulent flows. The present numerical results show a large shock-separated reversed flow region for the $R_p = 0.72$ case. The large separation bubble is caused by the use of the algebraic turbulence model which cannot adequately describe the turbulence field subjected to the streamline curvature and the normal shock. It is interesting to note that the k-ω turbulence model (ref. 10) also yields a largely separated flow region for the steady flow for $R_p = 0.72$. The objective of the present study is limited to the development and the verification of the time-accurate lower-upper factorization scheme, and optimization of the turbulence model is not attempted.

The time-accurate lower-upper factorization scheme shows a few important numerical aspects. A large amount of artificial dissipation can impair the numerical results and hence alternative artificial dissipation models have also been proposed (refs. 14 and 15). However, the present numerical method yields stable numerical results by using a much smaller artificial dissipation than other numerical methods (refs. 2, 3, 6, and 11). The method also yields a stable numerical result with the use of a large CFL number. The maximum CFL number that can be used to obtain stable numerical results for the present method is at least one order of magnitude greater than those for the other numerical methods (refs. 1, 6, and 11). Thus, the method is competitive with steady flow solvers for steady flows. For time-dependent flows, the time-step size is limited only by the physical phenomenon of the fluid flow to be considered.

REFERENCES

1. Jameson, A.; and Yoon, S.: LU Implicit Schemes with Multiple Grids for the Euler Equations - Lower-Upper Factorization. AIAA Paper 86-0105, Jan. 1986.

2. Shuen, J.S.: and Yoon, S.: Numerical Study of Chemically Reacting Flows Using an LU Scheme. AIAA Paper 88-0436, Jan. 1988.

3. Yu, S.-T., et al.: Numerical Simulation of Hypersonic Internal Flows with Equilibrium of Finite Rate Chemistry. AIAA Paper 88-0273, Jan. 1988.

4. Yoon, S.-K.; Kwak, D.; and Chang, L.: LU-SGS Implicit Algorithm for Three-Dimensional Incompressible Navier-Stokes Equations with Source Term. AIAA Paper 89-1964 June 1989.

5. Beam, R.M.; and Warming, R.F.: An Implicit Factored Scheme for the Compressible Navier-Stokes Equations. AIAA J., vol. 16, no. 4, 1978, pp. 393-402.

6. Towne, C.E., et al.: PROTEUS Two-Dimensional Navier-Stokes Computer Code - Version 1.0. NASA TM-102551, 1990.

7. Salmon, J.T.; Bogar, T.J.; and Sajben, M.: Laser Doppler Velocimeter Measurements in Unsteady, Separated, Transonic Diffuser Flows. AIAA J., vol. 21, no. 12, Dec. 1983, pp. 1690-1697.

8. Sajben, M.; Bogar, T.J.; and Krontil, J.C.: Forced Oscillation Experiments in Supercritical Diffuser Flow. AIAA J., vol. 22, no. 4, Apr. 1984, pp. 465-474.

9. Hsieh, T.; Wardlaw, Jr., A.B.; and Collins, P.: Numerical Investigation of Unsteady Inlet Flow Fields. AIAA J. vol. 25, no. 1, Jan. 1987, pp. 75-81.

10. Liou, M.-S.; and Coakley, T.J.: Numerical Simulations of Unsteady Transonic Flows in Diffusers. AIAA J., vol. 22, no. 8, Aug. 1984, pp. 1139-1145.

11. Pulliam, T.H.: Artificial Dissipation Models for the Euler Equations. AIAA J., vol. 24, no. 12, 1986, pp. 1931-1940.

12. Baldwin, B.S.; and Lomax, H.: Thin-Layer Approximation and Algebraic Model for Separated Turbulent Flows. AIAA Paper 78-257, 1978.

13. Kline, S.J.; Cantwell, B.J.; and Lilley, G.M., eds.: The 1980-1981 AFOSR-HTTM Stanford Conference on Complex Turbulent Flows, Vols. 1-3, Stanford, CA, 1981.

14. Dulikravich, G.; and Dorney, D.: Artificial Dissipation Sensors for Computational Gasdynamics. AIAA Paper 89-0643, Jan. 1989.

15. Merriam, H.L.: Towards a Rigorous Approach to Artificial Dissipation - In Computational Fluid Dynamics. AIAA Paper 89-0471, Jan. 1989.

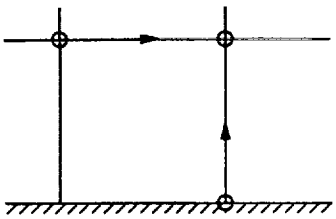

(a) Lower sweep.

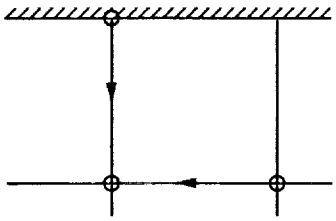

(b) Upper sweep.

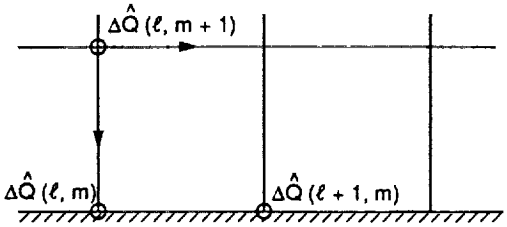

(c) $\Delta\hat{s}$ on the boundary.

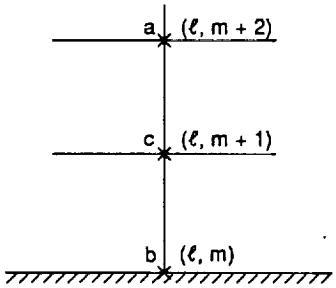

(d) Grid point on the boundary.

Figure 1. — Mesh near the boundary.

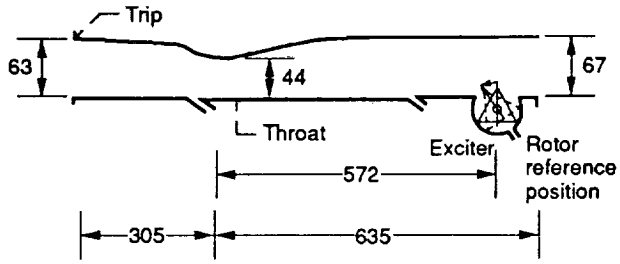

Figure 2. — Transonic flow channel. (All dimensions are in mm.)

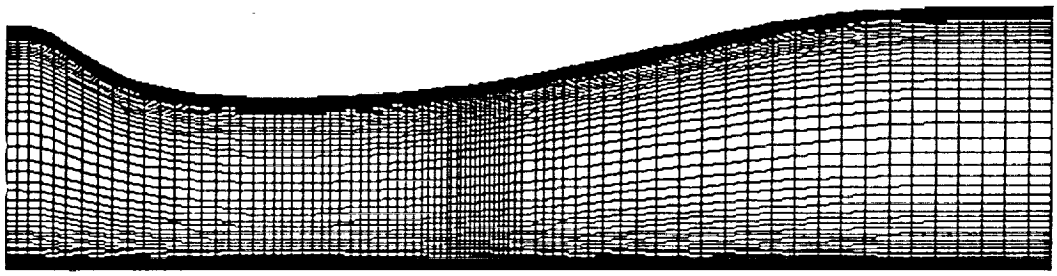

x/H = –2.7 x/H = 7.5

Figure 3. — Mesh in the vicinity of channel throat.

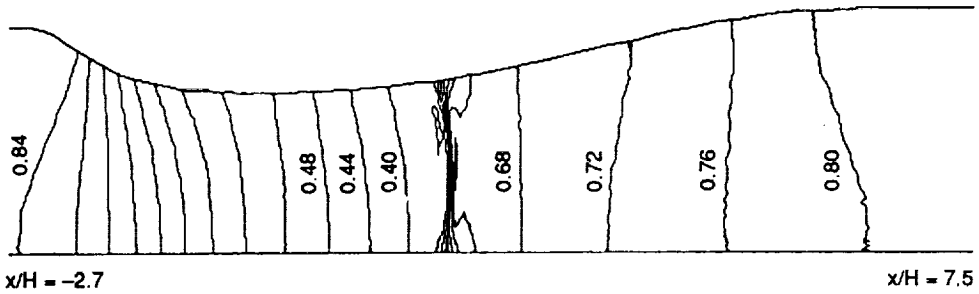

(a) Pressure.

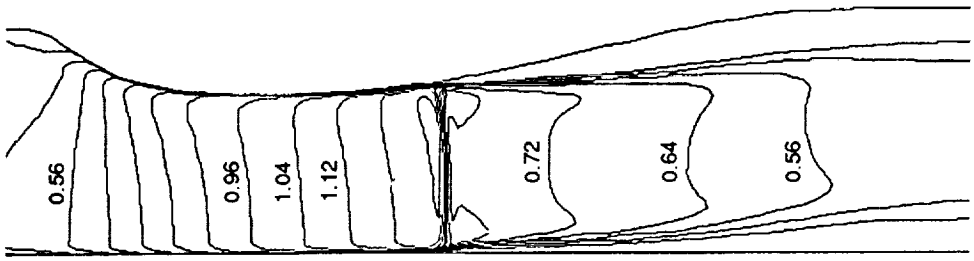

(b) Mach number.

Figure 4. — Contour plot of pressure and Mach number for $p_e/p_t = 0.82$.

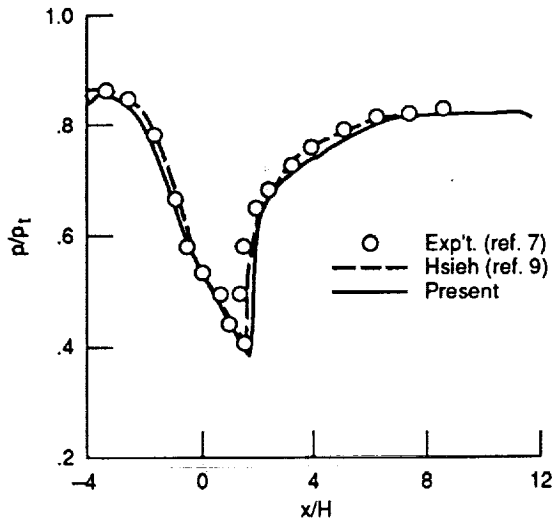

(a) Bottom wall.

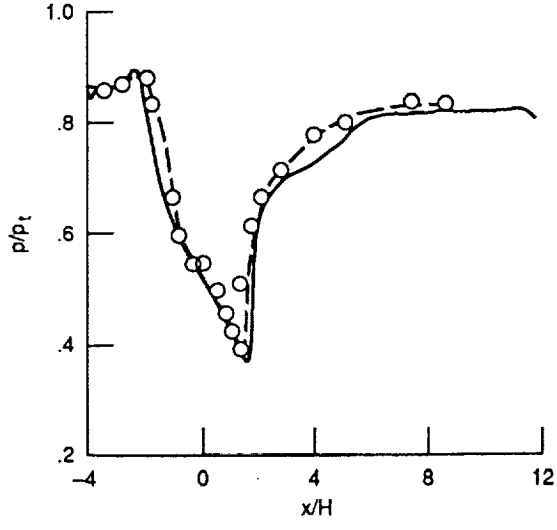

(b) Top wall.

Figure 5. — Pressure distributions for $p_e/p_t = 0.82$.

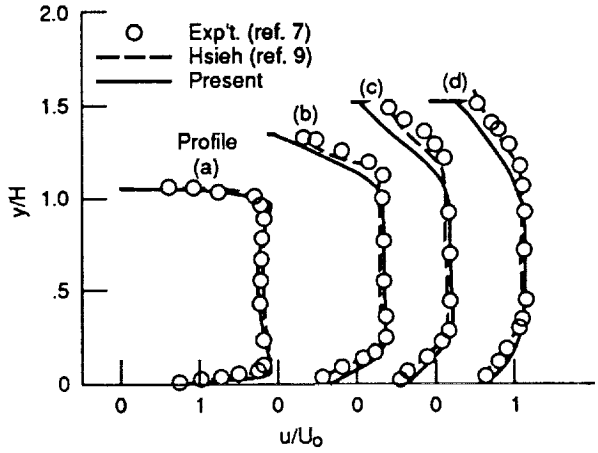

Figure 6. — Steady-state velocity profiles for $p_e/p_t = 0.82$. Profile (a), x/H = 1.73; (b), x/H = 4.04; (c), x/H = 6.34; (d) x/H = 8.36.

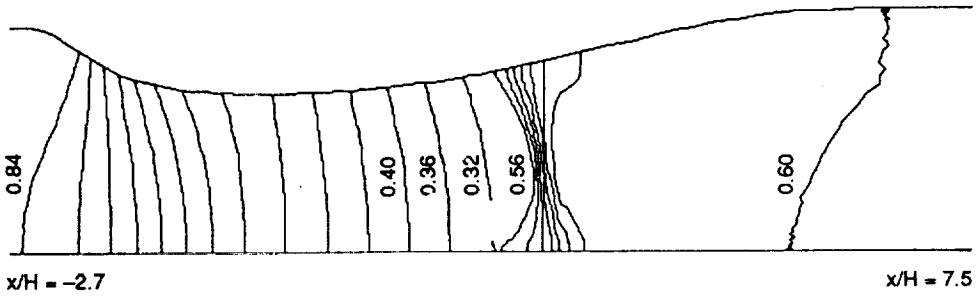

(a) Pressure.

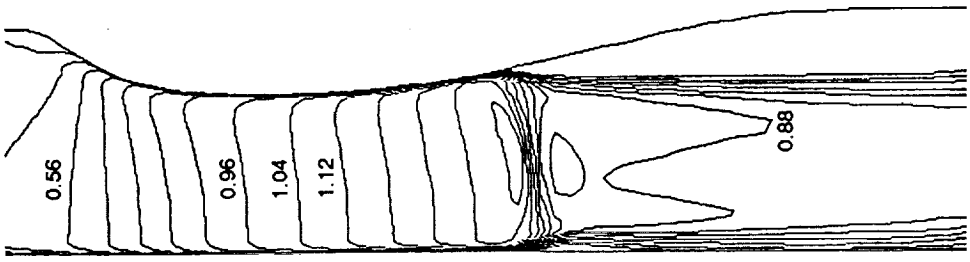

(b) Mach number.

Figure 7. — Contour plot of pressure and Mach number for $p_e/p_t = 0.72$.

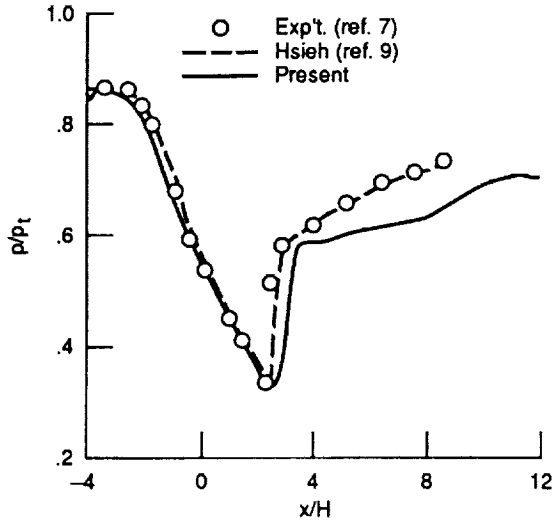

(a) Bottom wall.

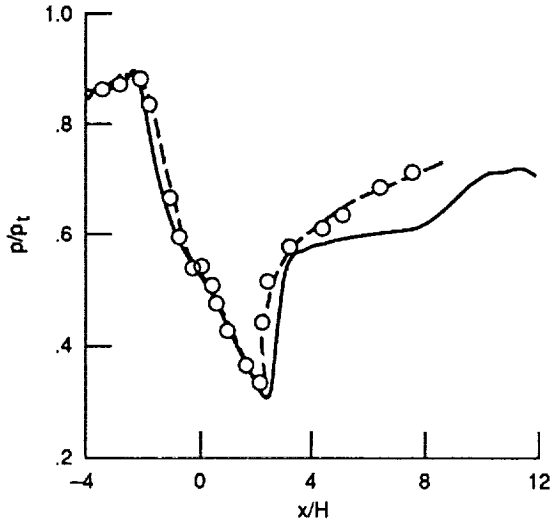

(b) Top wall.

Figure 8. — Pressure distributions for $p_e/p_t = 0.72$.

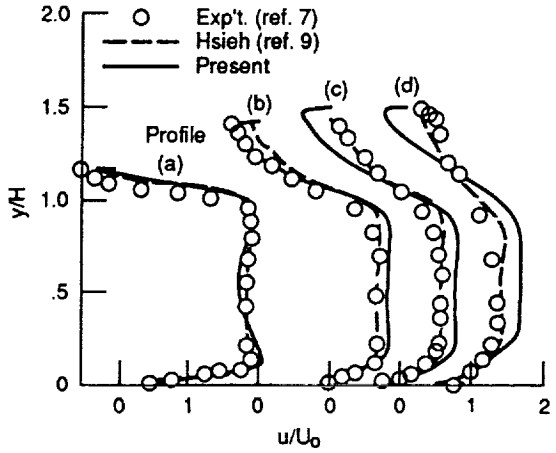

Figure 9. — Steady-state velocity profiles for $p_e/p_t = 0.72$. Profile (a), x/H = 2.89; (b), x/H = 4.61; (c), x/H = 5.76; (d) x/H = 8.36.

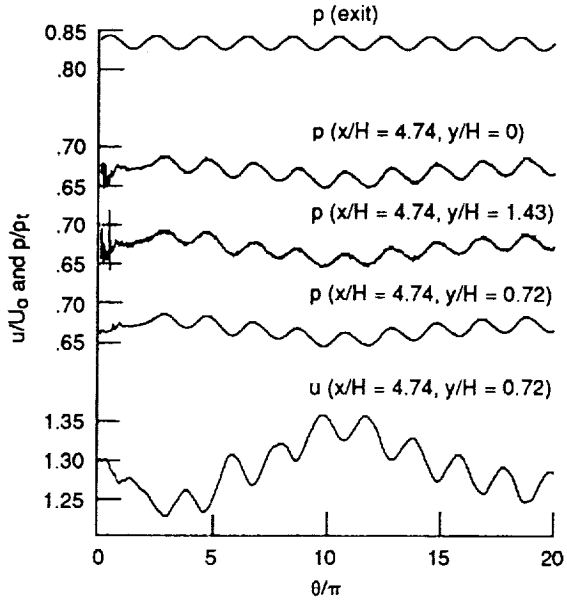

Figure 10. — Evolution of velocity and pressure in time for very weakly excited flow ($p_e = p_o + p_c \sin(2\pi fT)$; where $p_o = 0.82$, $p_c = 0.0082$, and f = 300).

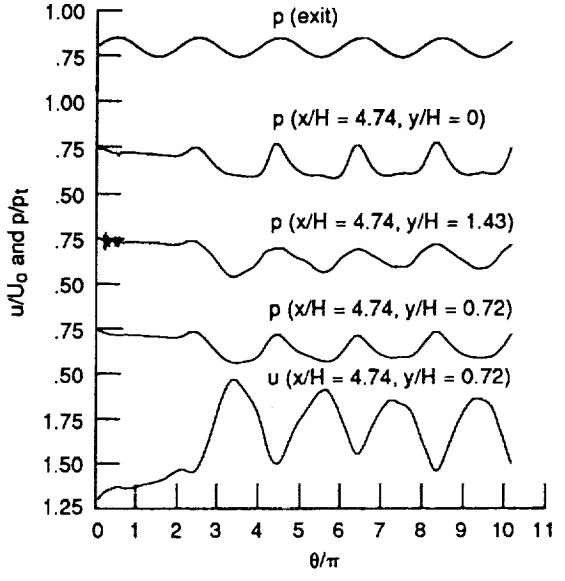

Figure 11. — Evolution of velocity and pressure in time for strongly excited flow ($p_e = p_o + p_c \sin(2\pi fT)$; where $p_o = 0.77$, $p_c = 0.05$, and f = 300).

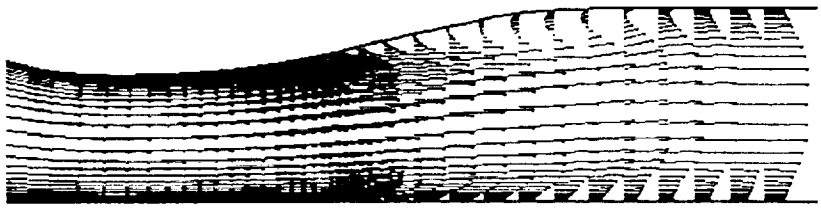

(a) $\theta = 8.0\ \pi$.

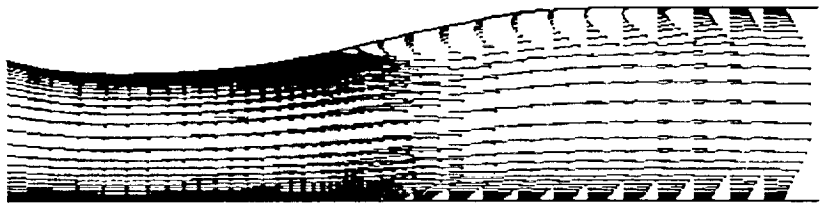

(b) $\theta = 8.5\ \pi$.

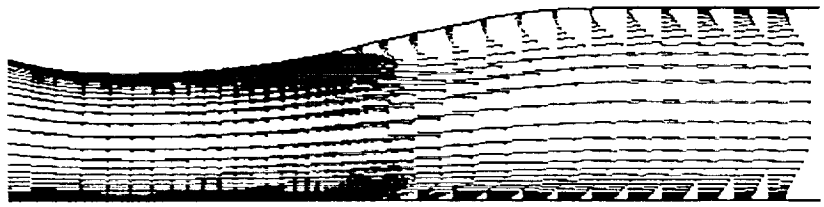

(c) $\theta = 9.0\ \pi$.

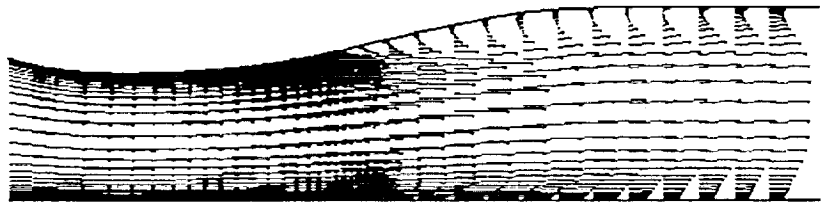

(d) $\theta = 9.5\ \pi$.

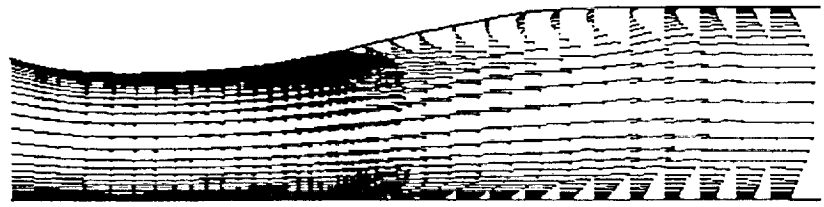

(e) $\theta = 10.0\ \pi$.

Figure 12. — Oscillatory motion of separated bubble for strongly excited flow.

NASA
National Aeronautics and Space Administration

Report Documentation Page

1. Report No.	2. Government Accession No.	3. Recipient's Catalog No.
NASA CR-187071		

4. Title and Subtitle
Calculations of Steady and Transient Channel Flows with a Time-Accurate L-U Factorization Scheme

5. Report Date
August 1991

6. Performing Organization Code

7. Author(s)
S.-W. Kim

8. Performing Organization Report No.
None (E-6018)

10. Work Unit No.
505-62-52

9. Performing Organization Name and Address
University of Texas at Arlington
Department of Aerospace Engineering
Arlington, Texas 76010

11. Contract or Grant No.
NCC3-180

13. Type of Report and Period Covered
Contractor Report
Final

12. Sponsoring Agency Name and Address
National Aeronautics and Space Administration
Lewis Research Center
Cleveland, Ohio 44135-3191

14. Sponsoring Agency Code

15. Supplementary Notes
Project Manager, Robert M. Stubbs, Internal Fluid Mechanics Division, NASA Lewis Research Center, (216) 433-6303.

16. Abstract
Calculations of steady and unsteady, transonic, turbulent channel flows with a time-accurate, lower-upper (L-U) factorization scheme are presented. The L-U factorization scheme is formally second-order accurate in time and space, and it is an extension of the steady-state flow solver (RPLUS) used extensively to solve compressible flows. A time-discretization method and the implementation of a consistent boundary condition specific to the L-U factorization scheme are also presented. The turbulence is described by the Baldwin-Lomax algebraic turbulence model. The present L-U scheme yields stable numerical results with the use of much smaller artificial dissipations than those used in the previous steady-flow solver for the steady and unsteady channel flows. The capability to solve time-dependent flows is shown by solving very weakly excited and strongly excited, forced oscillatory, channel flows.

17. Key Words (Suggested by Author(s))	18. Distribution Statement
Unsteady flow Transonic flow Turbulent flow L-U factorizations scheme	Unclassified - Unlimited Subject Category 34

19. Security Classif. (of the report)	20. Security Classif. (of this page)	21. No. of pages	22. Price*
Unclassified	Unclassified	18	A03

NASA FORM 1626 OCT 86

*For sale by the National Technical Information Service, Springfield, Virginia 22161